International Journal of Biological Macromolecules 283 (2024) 137904

Contents lists available at ScienceDirect

International Journal of Biological Macromolecules

journal homepage: www.elsevier.com/locate/ijbiomac

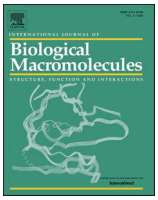

Exploring the conformational space of the mobile flap in *Sporosarcina pasteurii* urease by cryo-electron microscopy

Luca Mazzei [a,*,1], Giancarlo Tria [b,d,1], Stefano Ciurli [a], Michele Cianci [c,*]

[a] *Laboratory of Bioinorganic Chemistry, Department of Pharmacy and Biotechnology (FaBiT), University of Bologna, I-40138 Bologna, Italy*
[b] *Florence Center for Electron Nanoscopy (FloCEN), c/o Chemistry Department "Ugo Schiff", University of Florence, I-50019 Sesto Fiorentino, (FI), Italy*
[c] *Department of Agricultural, Food and Environmental Sciences, Polytechnic University of Marche, I-60131 Ancona, Italy*
[d] *National Research Council, Institute of Cristallography URT Caserta c/o University of Campania "Luigi Vanvitelli", I-81100 Caserta, Italy*

A B S T R A C T

To fully understand enzymatic dynamics, it is essential to explore the complete conformational space of a biological catalyst. The catalytic mechanism of the nickel-dependent urease, the most efficient enzyme known, holds significant relevance for medical, pharmaceutical, and agro-environmental applications. A critical aspect of urease function is the conformational change of a helix-turn-helix motif that covers the active site cavity, known as the mobile flap. This motif has been observed in either an *open* or a *closed* conformation through X-ray crystallography studies and has been proposed to stabilize the coordination of a urea molecule to the essential dinuclear Ni(II) cluster in the active site, a requisite for subsequent substrate hydrolysis. This study employs cryo-electron microscopy (cryo-EM) to investigate the transient states within the conformational space of the mobile flap, devoid of the possible constraints of crystallization conditions and solid-state effects. By comparing two cryo-EM structures of *Sporosarcina pasteurii* urease, one in its native form and the other inhibited by N-(*n*-butyl) phosphoric triamide (NBPTO), we have unprecedently identified an intermediate state between the *open* and the catalytically efficient *closed* conformation of the helix-turn-helix motif, suggesting a role of its tip region in this transition between the two states.

1. Introduction

Urease is a non-redox nickel-enzyme found in plants, algae, fungi, and various microorganisms. It plays a vital role in the global nitrogen cycle by catalyzing the hydrolytic decomposition of urea to give ammonia and carbamate. The resulting pH increase from this reaction is a primary factor in the adverse effects of urease activity on human and animal health, as well as agriculture [1]. Several human pathogens exploit urease as a virulence factor [2] including *Helicobacter pylori* [3], *Staphylococcus aureus* [4], *Mycobacterium tuberculosis* [5], *Cryptococcus neoformans* [6], and *Yersinia enterocolitica* [7]. Understanding the enzymatic mechanism of urease is thus crucial for developing effective drugs against these pathogens.

Current insights into the urease catalytic mechanism are based on a series of X-ray crystal structures of *Sporosarcina pasteurii* urease (SPU) in both native and inhibited states [1e,8]. Urea chelates the dinuclear Ni (II) cluster in the active site (Scheme 1) using the carbonyl O atom [bound to Ni(1)] and one of the two amido N atoms [bound to Ni(2)]. This binding, driven by hydrogen bonds from surrounding protein residues, activates the urea C atom for nucleophilic attack by the μ-hydroxo ligand (OH) bridging the two Ni(II) ions. The protonation of the distal C-NH_2 urea amide group, forming the C-NH_3^+ moiety, which eventually breaks down to ammonia and carbamate, involves the conserved residues αCys322 and αHis323 residues, located on a 30-residues helix-turn-helix motif covering the active site cavity. The role of αHis323 in catalysis has been debated, but recent density functional theory (DFT) calculations [9] suggest that the proximity of αHis323 to αCys322 increases the reactivity of the cysteine thiol, indicating that αCys322 and αHis323 could act as a catalytic dyad that protonates the distal C-NH_2 amide through a shared proton.

Regardless of the fine details of the proton transfer steps during urease catalysis, the critical role of the αCys322-αHis323 dyad emphasizes the importance of the conformational space of the helix-turn-helix motif that supports these residues. This motif has been observed in two distinct conformations, *open* or *closed*, depending on the native or inhibited state of the enzyme, the source of the enzyme, and the solution pH, and for this reason is also called *mobile flap*. The *open* conformation has been observed in native SPU, SPU bound to boric acid (a urea substrate analogue) [8c] and other inhibitors [8b,8d,10]. Moreover, an *open* flap has been found in SPU inactivated with 1,4-benzoquinone [11], catechols [12], hydroquinone [13], Ebselen [14], thiuram derivatives [9], and heavy metal ions such as Ag(I) [15] and Au(I) [16]; these

* Corresponding authors.
E-mail addresses: luca.mazzei2@unibo.it (L. Mazzei), giancarlo.tria@cnr.it (G. Tria), stefano.ciurli@unibo.it (S. Ciurli), m.cianci@univpm.it (M. Cianci).
[1] These authors contributed equally

https://doi.org/10.1016/j.ijbiomac.2024.137904
Received 10 September 2024; Received in revised form 12 November 2024; Accepted 19 November 2024
Available online 20 November 2024

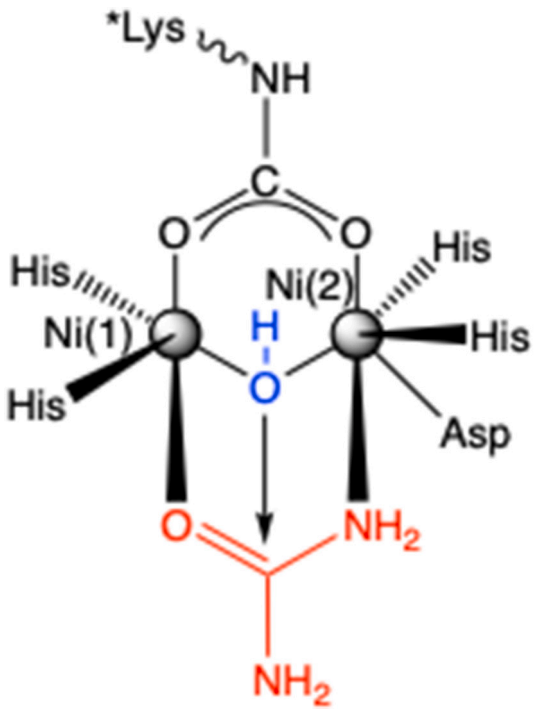

Scheme 1. Catalytic mechanism of urease

inactivators force the flap into an *open* conformation, supporting the idea that its closure is necessary for catalysis. In the *open* conformation, the αCys322-αHis323 dyad is located about 12–13 Å far from the binuclear center. In contrast, structures of SPU bound to the transition state analogues, such as diamidophosphate (DAP) and mono-amido thiophosphate (MATP), show a *closed* flap conformation [8a,8e,8f,8h], where the αCys322-αHis323 dyad moves closer to the dinuclear Ni(II) cluster, reducing the distance to *ca.* 4–5 Å. High-resolution (better than 2.5 Å) X-ray crystal structures of *Canavalia ensiformis* (jack bean) urease (JBU) bound to phosphate and native *Cajanus cajan* (pigeon pea) urease (PPU) also show an *open* flap [17]. An exception is *Klebsiella aerogenes* urease (KAU), for which all reported X-ray structures show a *closed* flap conformation [18], except for a Cys-to-Tyr mutant in which the flap was modeled in an *open* conformation justified by the steric hindrance of the tyrosine aromatic ring [18c].

The conformational variability of the helix-turn-helix motif has been tentatively explained by two hypothesis: 1) the extended interactions made by the flap favor flap closure, but side chains and water in the urea binding pocket destabilize the *closed* state of the native enzyme [19], or 2) the stabilization of the flap in an *open* or *closed* state is influenced by pH, promoting an *open* conformation at acidic-to-neutral pH and a *closed* conformation at neutral-to-alkaline pH [8f,8h]. The *open/closed* conformational change of the helix-turn-helix motif is proposed to gate substrate and products passage in the *open* state while stabilizing the substrate and/or intermediate during catalysis in the *closed* state [8f,8h].

To determine whether the distinct conformations of the mobile flap observed in X-ray crystallography studies are due to solid-state packing within the crystallographic lattice, we explored the conformational space for this motif in SPU using cryo-electron microscopy (cryo-EM). This technique allows the observation of all possible protein conformers in solution. Four urease structures have been determined using cryo-EM: native *Yersinia enterocolitica* urease (YEU, 1.2 MDa for a $[(\alpha\beta\gamma)_3]_4$ quaternary structure) [20], two ligand-bound *Helicobacter pylori* urease forms (HPU, 1.2 MDa for a $[(\alpha\beta)_3]_4$ assembly) [21], and the phosphate-bound form of JBU (*ca.* 0.5 MDa due to its $[(\alpha)_6]_2$ quaternary structure) [22]. All these structures show the mobile flap in the *open* conformation. SPU, with a $(\alpha\beta\gamma)_3$ quaternary structure and a mass of approximately 0.25 MDa, presents a challenge for cryo-EM due to its smaller particle size.

In this study, we report two cryo-EM structures of SPU: one in its native state and the other bound to diamidophosphate (DAP), obtained after incubation with N-(*n*-butyl) phosphoric triamide (NBPTO) [1e,8]. NBPTO is a potent urease inhibitor belonging to the phosphoramides class, that operates *via* a slow-binding mechanism that appears to involve an initial hydrolytic cleavage of the P-NH-(*n*-butyl) amide moiety, catalyzed *in situ* by urease. This step results in the release of *n*-butylamine and DAP. The latter is a tetrahedral moiety that mimics the transition state formed during the enzymatic urea hydrolysis, and is trapped in the active site upon binding to the dinuclear cluster of Ni(II) and effectively blocking the catalytic activity [1e,8]. These structures provide new insights into the role of the apical portion of the helix-turn-helix motif in enzyme catalysis.

2. Results and discussion

2.1. Data analysis of cryo-EM data

Single particle cryo-EM was utilized to determine the structures of both native and NBPTO-inhibited SPU. For both structures, images were processed through iterative rounds of reference-free two-dimensional (2D) (Fig. 1A,B) and three-dimensional (3D) classification to select particles suitable for 3D reconstruction. Despite the three-fold symmetry of the urease assembly and the tilted image data collection strategy employed, preferential orientations were observed in the 2D class averages (Fig. 1C,D), a phenomenon also noted in the cryo-EM structure of YEU [20]. The Coulomb potential density maps for native and NBPTO-inhibited SPU achieved similar global resolutions of 3.12 Å and 2.92 Å, respectively (Fig. 1E,F). Local resolution estimates for the two cryo-EM maps indicate that most protein regions exhibit resolutions equal to or better than the nominal resolution, while solvent-exposed areas show greater variability (Fig. 1G,H).

2.2. Cryo-EM structure of native SPU

Consistent with the crystallographic observations, the single-particle cryo-EM structures of native and NBPTO-inhibited SPU reveal a complete assembly of 0.25 MDa organized into a regular triangle-shaped trimer with sides measuring approximately 115 Å (Fig. 2A). Each trimer is a T-shaped oligomer of the type (αβγ), with the α, β, and γ subunits comprising 570, 126, and 100 residues, respectively. The high quality of both the cryo-EM maps allowed for the complete reconstruction of the α and γ chains (residues 1–570 and 1–100, respectively), and accurate modeling of residues 5–126 of the β chain. The cryo-EM maps of both native and NBPTO-inhibited SPU show significantly lower local resolution in the mobile flap region, making modeling of residues 311–340 of the α chains more challenging. Model-based local density sharpening of the cryo-EM maps, performed using LocScale [23], improved the quality of the map contrasts and allowing for unbiased interpretation and models reconstruction (Figs. 2B,C and 1-SI). The Coulomb potential density maps corresponding to residues 1–4 of the β chain of both native and NBPTO-inhibited SPU were not detectable, indicating significant flexibility in this N-terminal region; these residues are also absent in all X-ray crystal structures of SPU to date.

The two fully refined structures provide detailed insights into the overall folding of each polypeptide chain, which largely aligns with structural features previously inferred from X-ray crystallography studies [8d,24]. Each α chain forms the larger portion of the T-shaped long arm of one αβγ trimer; by interacting with the two α chains from the other trimers, it forms the disk-shaped core of the full assembly; the α chain consists of a large $(\alpha\beta)_8$-barrel domain and a C-terminal β-type domain. Each β chain constitutes the smaller portion of the T-shaped long arm of one αβγ trimer and is located at the vertices of the full assembly; it features a β strand-rich N-terminal region and a C-terminal

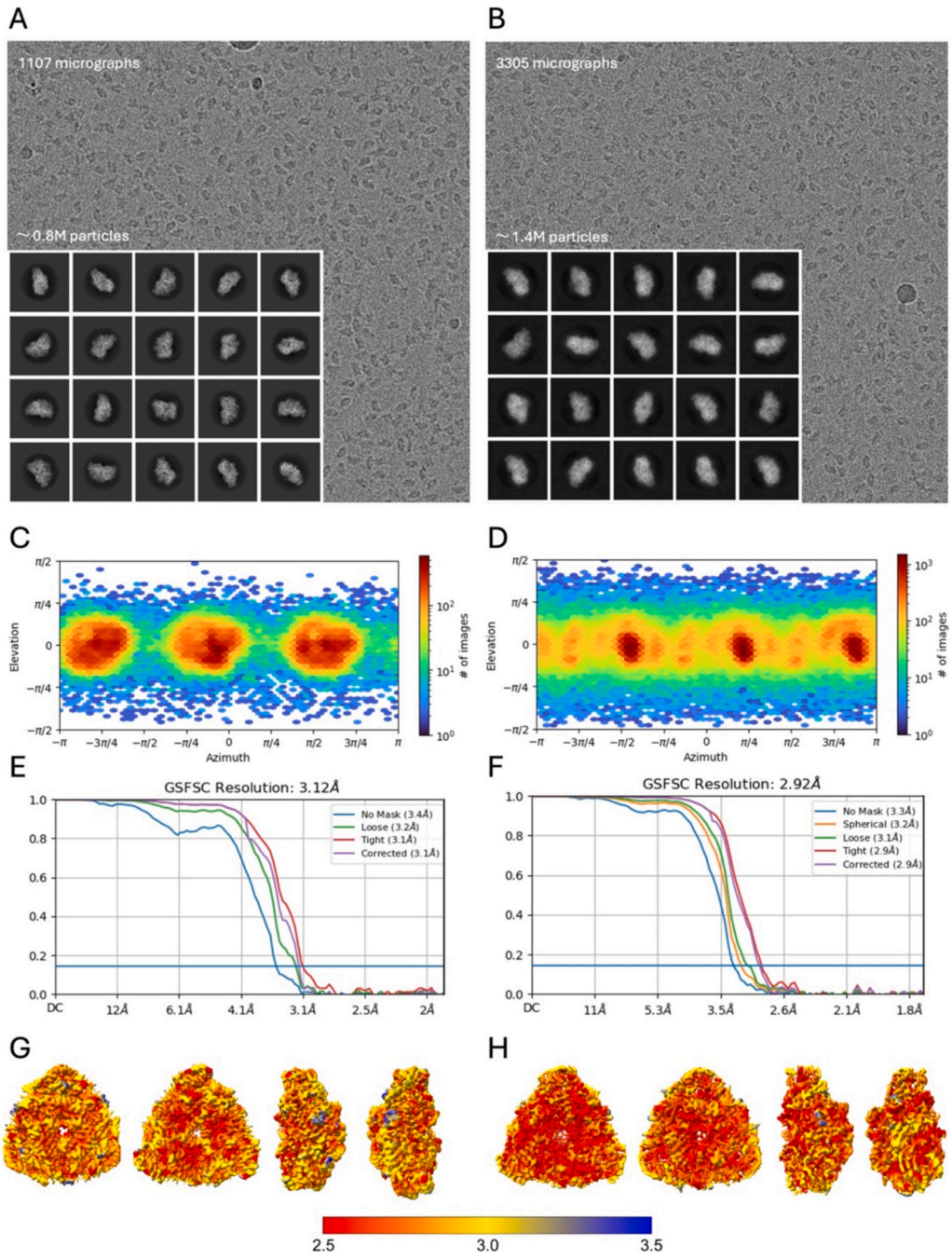

Fig. 1. Cryo-EM reconstructions of native (panels A, C, E, G) and NBPTO-inhibited SPU (panels B, D, F, H). Representative micrographs (A, B) at a defocus of −2.2 μm for the native and −1.8 μm for the NBPTO-inhibited derivative, with insert of representative 2D classes. Orientation plots (C, D) showing the distribution of orientations for each dataset. Fourier Shell Correlation (FSC) plots (E, F). The resolution is reported at the gold standard FSC value of 0.143. Local resolution coloring of the reconstructed volume shown as surface representation at four different orientations (G, H). The figures were generated using ChimeraX and contoured at RMSD = 3.5. Local resolution range scale is shown.

α-helix of approximately 12 residues, with the C-terminal α-helix forming the extremity of each assembly vertex. Each γ subunit, representing the short arm of each T-shaped αβγ trimer, is located on the top face of the full protein; it facilitates the assembly by interacting with the parent α chain and symmetry-related γ chains; the γ subunit is composed of four N-terminal α helices and two C-terminal antiparallel β strands. This refined cryo-EM structures expose the intricate organization and interactions within the SPU trimer, offering a comprehensive view that complements previous crystallographic data.

2.3. Cryo-EM structure of native SPU

The 3.12-Å global resolution of the cryo-EM map of native SPU enabled detailed visualization of the structural features of the enzyme active site pocket, including the localization of the dinuclear Ni(II) metallo-center and a comprehensive description of its coordination environment (Fig. 2D). Each active site resides in a 20-Å deep cleft of the α chain, positioned at the edge of the parent αβγ trimer and nestled between the α chain and a β chain of the adjacent αβγ trimer in the assembly. The active site contains two Ni(II) ions, separated by 3.6 Å, both coordinated by the bridging carbamylated sidechain of αLys220. Ni(1) is

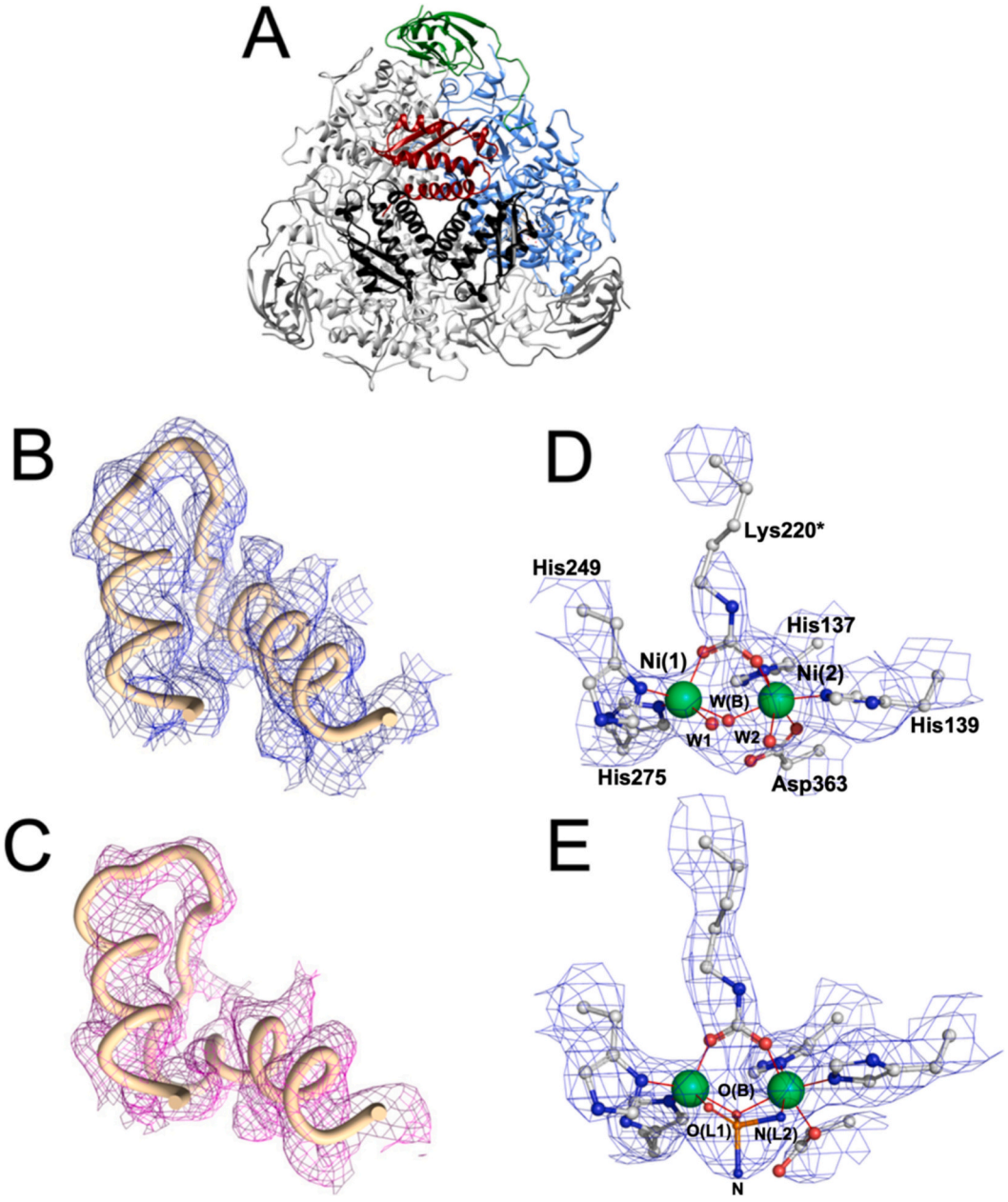

Fig. 2. *Sporosarcina pasteurii* urease. (A) Ribbon representation of the reconstructed triangle-shaped SPU biological assembly: one (αβγ) T-shaped trimer displays the α, β, and γ chains colored in cornflower blue, green, and red, respectively, while the other two hetero-trimers are shown in shades of gray. (B and C) Region of the mobile flap for native (B) and NBPTO-inhibited (C) SPU reconstructed after LocScale map sharpening. LocScale maps are shown contoured at 5 RMSD. (D and E) Active site and Ni(II)-coordination environment of native (D) and NBPTO-inhibited (E) SPU, respectively. A, B, and C were generated using ChimeraX, D and E were generated using PyMOL.

further coordinated by the sidechains of αHis249 and αHis275, while Ni (2) is bound to αHis137, αHis139, and αAsp363. A well-ordered hydroxide ion, W(B), symmetrically bridges the two Ni(II) ions and was modeled into the Coulomb potential detectable between them. Additionally, two proximal solvent molecules (W1 and W2) were successfully modeled in front of Ni(1) and Ni(2), respectively, making Ni(1) pentacoordinated in a pseudo-tetragonal pyramidal geometry and Ni(2) hexacoordinated in a pseudo-octahedral geometry. A fourth distal solvent molecule, typically seen in X-ray crystal structures and completing a tetrahedral cluster of solvent molecules, was not visible and thus was not modeled. A full list of distances and angles is provided in Table 1, where W1, W2, and W(B) are listed as L_1, L_2, and L_B, respectively.

The refined cryo-EM structure of native SPU closely matches the structure determined by X-ray crystallography (PDB code: 4CEU) [8d] (global RMSD values between their backbone atoms is shown in Table 2-SI). A more detailed per-residue RMSD analysis reveals that the α, β, and γ chains of the two compared structures have largely invariant backbones (Fig. 3A). Slightly larger RMSD values are observed in the mobile flap region (residues 310–340 of the α chain); the cryo-EM reconstructed model, however, successfully overlaps to that of the X-ray crystal structure, thus adopting an *open* conformation. This region also exhibits the largest Atomic Displacement Parameters (ADPs) (Fig. 2-SI), thus indicating intrinsic mobility. The obtained cryo-EM structure of native SPU confirms the viability of this technique for achieving high-quality information for a protein of this relatively small size.

Table 1
Selected distances and angles around the Ni(II) ions in the cryo-EM structures of native and DAP-bound SPU.

Ni - L Distances (Å)	Native (9GML)	DAP-bound (9GNR)
Ni(1) - αLys220* Oθ1	2.0	1.9
Ni(1) - L_B	2.0	2.0
Ni(1) - L_1	2.1	2.0
Ni(1) - αHis249 Nδ	2.0	2.0
Ni(1) - αHis275 Nε	2.0	2.0
Ni(2) - αLys220* Oθ2	2.0	2.0
Ni(2) - L_B	2.0	2.1
Ni(2) - L_2	2.2	2.0
Ni(2) - αHis137 Nε	2.0	2.0
Ni(2) - αHis139 Nε	2.0	2.0
Ni(2) - αAsp363 Oδ1	2.0	2.1
Ni(1) ••• Ni(2)	3.6	3.5
L_1 ••• L_2	2.3	2.6
L - Ni - L Angles (°)		
αLys220* Oθ1 - Ni(1) - αHis249 Nδ	101.7	105.2
αLys220* Oθ1 - Ni(1) - αHis275 Nε	99.8	104.8
αLys220* Oθ1 - Ni(1) - L_B	89.2	94.6
αLys220* Oθ1 - Ni(1) - L_1	108.4	107.3
αHis249 Nδ - Ni(1) - αHis275 Nε	98.6	95.3
αHis275 Nε - Ni(1) - L_B	95.8	89.9
L_B - Ni(1) - L_1	69.2	78.3
L_1 - Ni(1) - αHis249 Nδ	91.4	85.4
αHis249 Nδ - Ni(1) - L_B	160.0	177.2
αHis275 Nε - Ni(1) - L_1	147.4	146.5
αLys220* Oθ2 - Ni(2) - αHis137 Nε	84.2	80.9
αLys220* Oθ2 - Ni(2) - αHis139 Nε	96.3	90.6
αLys220* Oθ2 - Ni(2) - L_2	93.7	92.3
αLys220* Oθ2 - Ni(2) - L_B	84.6	94.8
αAsp363 Oδ1 - Ni(2) - αHis137 Nε	82.7	95.9
αAsp363 Oδ1 - Ni(2) - αHis139 Nε	83.9	82.2
αAsp363 Oδ1 - Ni(2) - L (2)	100.5	92.0
αAsp363 Oδ1 - Ni(2) - L_B	101.6	93.8
L_2 - Ni(2) – L_B	65.0	79.2
L_B - Ni(2) - αHis137 Nε	93.3	92.3
αHis137 Nε- Ni(2) - αHis139 Nε	113.6	107.6
αHis139 Nε- Ni(2) - L (2)	88.1	81.3
αLys220* Oθ2 - Ni(2) - αAsp363 Oδ1	165.8	180.0
L_B - Ni(2) - αHis139 Nε	153.1	160.1
L_2- Ni(2) - αHis137 Nε	158.3	168.7
Ni(1) - L_B - Ni(2)	130.1	119.0

2.4. Cryo-EM structure of inhibited SPU

The 2.92-Å cryo-EM structure of NBPTO-inhibited SPU revealed the architecture of the Ni(II)-containing active site and the coordination environment of the two metal ions having strong consistency with the native enzyme (Fig. 2E), except for a tetrahedron-shaped, large Coulomb potential density detected near the Ni(II) ions. This density was successfully interpreted as a molecule of DAP, resulting from the well-established enzyme-catalyzed hydrolysis of NBPTO.

The binding pose of DAP to the nickel metallo-center closely matches that previously reported by X-ray crystal structures of SPU bound to DAP [8a,8f,8h]. In these structures, the ligand displaces the tetrahedral cluster of solvent molecules and completes the coordination environment of the Ni(II) ions by binding through one O atom to Ni(1) and one N atom to Ni(2) (L_1 and L_2 in Table 1, respectively). The second DAP oxygen atom (O_B) symmetrically bridges the Ni(1) and Ni(2) ions (L_B in Table 1), while the second N atom points away from the nickel metallo-center toward the active site cavity opening.

The refined cryo-EM structure of DAP-bound SPU was compared to the corresponding X-ray crystal structure determined at pH 7.5 (PDB code: 6RKG) [8f] as well as to the X-ray crystal structure and cryo-EM structure of native SPU (an analysis of the global RMSD between their backbone atoms is shown in Table 2-SI). The per-residue RMSD values indicate that the α, β, and γ chains have largely invariant backbones across all compared structures (Fig. 3B,C), with the exception of the mobile flap region, which also reflects in higher ADP values (Fig. 2-SI).

An in-depth analysis of the positioning of the helix-turn-helix motif with respect to the comparing structures revealed that the overall orientation of the two α-helices comprising residues 311–320 and 330–340 resembled the *open* conformation of the flap. However, the tip region of the first α-helix, corresponding to residues 320–323, unwinds, resulting in the movement of the αCys322-αHis323 dyad toward the bimetallic Ni(II)-cluster, as shown by the superimposition of the cryo-EM structures of native and DAP-inhibited SPU (Fig. 4). The flap conformation revealed by the cryo-EM structure of the DAP-bound SPU is unprecedented and indicates the viability of a wider conformational space for this critical motif.

Overall, the analysis of the cryo-EM maps of both native and the DAP-inhibited SPU indicates that the achieved resolution enables the identification of key structural features, such as minor conformational changes in the helix–turn–helix motif and facilitates comparisons between structures obtained from cryo-EM and X-ray diffraction data. The intermediate conformation observed in the cryo-EM structure of urease indicates a potential pathway for effecting the key movement of the helix-turn-helix motif, transitioning it from an *open* state to a catalytically efficient *closed* conformation.

The quality of the obtained Coulomb density maps, while generally high, allowed for the reasonably accurate positioning of small ligands, such as the bound DAP molecule within the active site. However, it is important to note that the resolution limitations inherent to cryo-EM, particularly for smaller molecules, introduce some degree of uncertainty in exactly defining the orientation and interactions of the ligand. Despite these challenges, the maps still provided sufficient detail to indicate key binding interactions, which are validated by a comparison with the higher resolution X-ray structures.

The results from applying cryo-EM to a system like urease, whose structures have been extensively studied through X-ray crystallography, highlight the value of using these two techniques in a complementary fashion. Cryo-EM offers a distinct advantage by being less affected by solid-state effects compared to crystallography, allowing for a more accurate representation of the macromolecule in its native solution state.

This result opens new opportunities for structure-based drug design, particularly by enabling the identification of an additional transient key binding site and allosteric region, consequently facilitating the development of inhibitors targeting urease, aiding in the rational design of novel therapeutic compounds. The ability to capture intermediate conformations in cryo-EM, demonstrated in this study, offers a valuable tool for studying the mechanisms of enzymes with similar molecular masses, providing deeper insights into their catalytic cycles and dynamic structural changes, which may lead to more effective strategies for modulating enzymatic activity.

3. Materials and methods

3.1. Sample preparation

Sporosarcina pasteurii urease (SPU) (molecular mass = 250 kDa), obtained in a pure form from *Sporosarcina pasteurii* DSM 33 cells [10d], was used at a final concentration of 2 mg mL^{-1} in 50 mM HEPES buffer, at pH 7.5, in the absence or in the presence of 5 mM N-(*n*-butyl) phosphoric triamide (NBPTO). Incubation of SPU in the presence of NBPTO (dissolved in the same buffer) occurred for three hours at room temperature.

3.2. Cryo-EM grid preparation, data collection and processing

Cryo-EM grids were prepared by dispensing ~3 μL of each sample on freshly glow-discharged grids (Quantifoil® R1.2/1.3300 Mesh Cu, Germany) kept at 100 % humidity and 10 °C, blotted with filter paper for 2 s and quickly plunge-frozen in liquid ethane using a Vitrobot Mark IV (Thermo Scientific) in order to allow the formation of a thin layer of amorphous ice containing embedded protein particles.

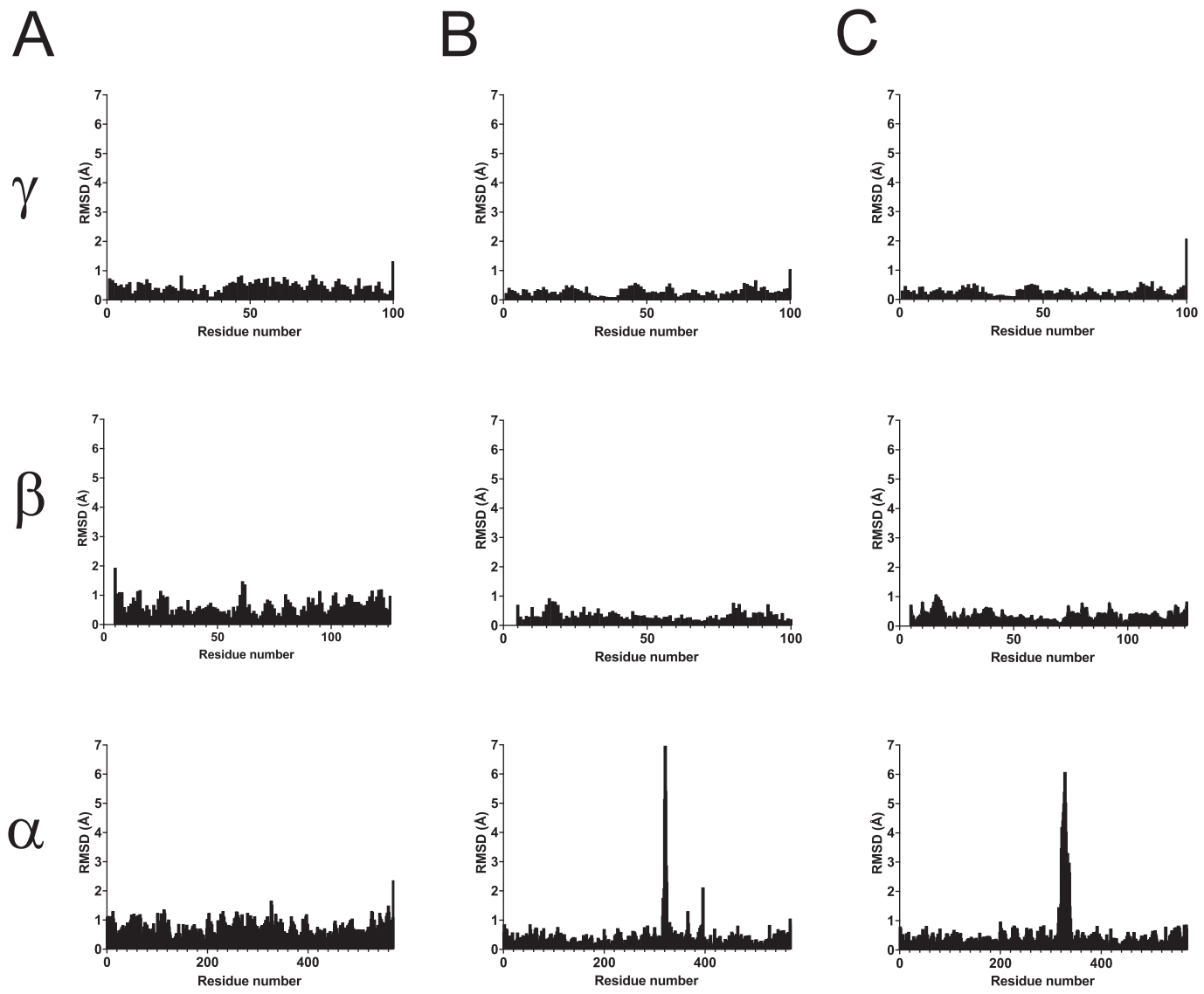

Fig. 3. Pairwise root mean square deviation (RMSD) per residue of SPU. The region belonging to the mobile flap is comprised in the 310–340 residue range of the α subunit. (A) Comparison between the γ, β and α chains of the Cryo-EM structure of native SPU and the X-ray crystal structure of native SPU (PDB code: 4CEU). (B) Comparison between the γ, β and α chains of the cryo-EM structure of DAP-bound SPU and the X-ray crystal structure of native SPU (PDB code: 4CEU). (C) Comparison between the γ, β and α chains of the cryo-EM structure of DAP-bound SPU and the X-ray crystal structure of DAP-bound SPU (PDB code: 6RKG).

Data of native SPU were recorded at the Florence Center for Electron Nanoscopy (FloCEN c/o Department of Chemistry "Ugo Schiff", University of Florence, Italy) using a Glacios microscope (Thermo Scientific) equipped with X-FEG high-brightness gun at 200 kV. Nominal magnification was set at ×150 k for a calibrated pixel size of 0.96 Å. The microscope was equipped with a Falcon 3 camera (Thermo Scientific) operated in electron counting mode and movies were recorded *via* the EPU control software (Thermo Scientific). A total dose of ~30 $e^-/Å^2$ was spread over 25.58 s of exposure time and 30 frames, resulting in a calibrated dose of ~1.09 e^-/pixel/frame. Defocus values were set in a range between −0.8 μm and − 2.2 μm, with 0.2 μm step. Data were collected a five different stage tilt-angle (0°, 10°, 20°, 30°, and 40°) for a total of 3035 movies.

Data of SPU inhibited by NBPTO were recorded at the CM01 facility of the European Synchrotron Radiation Facility (ESRF, Grenoble, France) using a Krios G3i microscope (Thermo Scientific) at 300 kV and nominal magnification of ×165 k for a calibrated pixel size of 0.827 Å. The microscope was equipped with a Gatan K3 direct electron detector operated in electron counting mode. A total dose of ~30 $e^-/Å^2$ was spread over 3.2 s of exposure time and 32 frames, resulting in a calibrated dose of 0.68 e^-/pixel/frame. Defocus values were set in a range between −0.8 μm and − 2.2 μm, with 0.2 μm step. Data were collected a two different stage tilt-angles (0° and 30°) for a total of 7785 movies (6444 and 1341 at 0° and 30°, respectively). As for the data collection on native urease before, this was deemed necessary to harness all the possible orientations of the SPU particles.

Preprocessing data analysis (patch motion correction, patch Contrast Transfer Function (CTF), reference-free particle picking, particle extraction, and two-dimensional (2D) classifications was performed in cryoSPARC v.4.2.1 [25] using a box size of 256 pixels. The resulting 2D classes were manually filtered and hence used for template picking. Movies showing a frame motion ≤10 pixels, astigmatism <800 Å, and a relative ice thickness between 95 and 105 nm were considered for further analysis. Aligned micrographs with CTF Thon rings fit estimated ≤4 Å for native SPU and ≤ 3.2 Å for NBPTO-treated SPU were further selected, resulting in final datasets consisting of 1177 and 3055 micrographs, respectively. A total of *ca.* 0.8 M and 1.4 M particles for native SPU and NBPTO-inhibited SPU, respectively, were used as initial particle stack for iterative 2D classification tasks. The three-dimensional (3D) Coulomb density maps corresponding to the complete trimeric

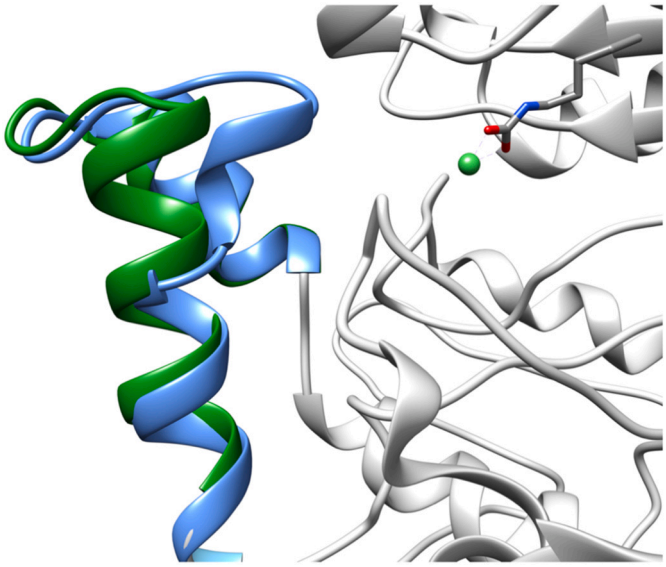

Fig. 4. Superimposition of the mobile flap regions for the native and the DAP-bound SPU structures colored in forest green and cornflower blue, respectively.

assemblies of urease were obtained by using the non-uniform refinement routine in cryoSPARC [26] with per particle CTF estimation and aberration correction while imposing a C_3 symmetry. After several 3D refinements, as well as local refinements following the cryoSPARC workflow, no further improvements were observed, and the final map resolutions were estimated in 3.12 Å and 2.92 Å for the native and the NBPTO-inhibited SPU, respectively. Estimation of global average resolution (Fourier shell correlation, FSC = 0.143) as well as focused resolution and sharpening were performed using cryoSPARC. The entire set of processing statistics for both the datasets are given in Table 1-SI.

3.3. Model building and refinement

The structural model of SPU as a $(\alpha\beta\gamma)_3$ trimer of trimers was reconstructed using ChimeraX [27] starting from the X-ray crystal structural model of SPU inhibited by catechol determined at 1.50 Å [12a] (PDB code: 5G4H), the highest resolution structure available showing the mobile flap in the *open* conformation. The PHENIX suite [28] was used for the subsequent steps. The $(\alpha\beta\gamma)_3$ trimer was docked into cryo-EM density maps using Dock-in-Map routine [28]. The density maps were sharpened initially using the *auto_sharpen* routine [29]. The map symmetry operators were calculated from the sharpened density maps using the *map_symmetry* routine searching for C_3 symmetry identified with a correlation of symmetry-related regions of 0.97. Subsequently, the unique part of the map and of the model was cut-out using the *map_box* routine. Iterative rounds of manual model rebuilding and refinement were conducted using COOT v.0.9.3 [30] and the *real_space_refine* routine [28], respectively. At a later stage of rebuilding, the $(\alpha\beta\gamma)_3$ trimer was reassembled using ChimeraX [27] to calculate a sharpened map using LocScale [23] available within the CCPEM suite [31] and improve maps in the mobile flap region. Default input parameters were applied to compute both *auto_sharpen* and LocScale maps. After complete model reconstruction, structural validation was performed using MolProbity [32] available in the PHENIX package. The entire set of refinement and validation statistics are given in Table 1-SI. Figures were prepared using ChimeraX [27] and PyMOL (The PyMOL Molecular Graphics System, Version 1.2r3pre, Schrödinger, LLC). The cryo-EM maps were deposited in the Electron Microscopy Data Bank with accession codes EMD-51450 and EMD-51478 for the cryo-EM maps of native and the DAP-bound SPU, respectively. Atomic model coordinates of the refined structures were deposited in the Protein Data Bank with accession numbers 9GML and 9GNR for native SPU and the DAP-bound SPU, respectively.

CRediT authorship contribution statement

Luca Mazzei: Writing – review & editing, Validation, Methodology, Conceptualization. **Giancarlo Tria:** Writing – original draft, Visualization, Methodology, Data curation, Conceptualization. **Stefano Ciurli:** Writing – review & editing, Supervision, Funding acquisition, Conceptualization. **Michele Cianci:** Writing – review & editing, Writing – original draft, Validation, Project administration, Formal analysis, Data curation, Conceptualization.

Funding sources

SC and LM acknowledge the support of Consorzio Interuniversitario di Risonanze Magnetiche di Metallo-Proteine (CIRMMP) and the University of Bologna. This study was carried out within the Agritech National Research Center and received funding from the European Union Next-GenerationEU (PIANO NAZIONALE DI RIPRESA E RESILIENZA (PNRR) – MISSIONE 4 COMPONENTE 2, INVESTIMENTO 1.4 – D.D. 1032 17/06/2022, CN00000022). This manuscript reflects only the authors' views and opinions, neither the European Union nor the European Commission can be considered responsible for them. MC's research is funded by Ricerca Scientifica di Ateneo (RSA2021–2023) program by Università Politecnica delle Marche. GT research is supported by the PNRR infrastructure project "Potentiating the Italian Capacity for Structural Biology Services in Instruct Eric (ITACA.SB)" (Project No. IR0000009, CUP B53C22001790006) within the call MUR 3264/2021 PNRR M4/C2/L3.1.1, funded by the European Union NextGenerationEU. Cryo-EM data were collected at the Florence Center for Electron Nanoscopy (FloCEN), Chemistry Department, University of Florence, Sesto Fiorentino (FI), and at the Cryo-EM facility CM01 at the European Synchrotron radiation Facility (Grenoble, France), beamtime award number MX-2262. We thank both the facility for the beam time and Dr. Eaazhisai Kandiah (ESRF) for the technical support.

Declaration of competing interest

The authors declare the following financial interests/personal relationships which may be considered as potential competing interests: Giancarlo Tria reports financial support was provided by European Union. Luca Mazzei reports equipment, drugs, or supplies was provided by European Union. Cianci Michele reports a relationship with Elettra Sincrotrone Trieste SCpA that includes: consulting or advisory. If there are other authors, they declare that they have no known competing financial interests or personal relationships that could have appeared to influence the work reported in this paper.

Appendix A. Supplementary data

Cryo-EM data collection, refinement and validation statistics, and additional structural analysis is available free of charge on-line. Supplementary data to this article can be found online at [doi:https://doi.org/10.1016/j.ijbiomac.2024.137904.]

Data availability

Data will be made available on request.

References

[1] [a] R.P. Hausinger, Microbiol. Rev. 51 (1987) 22–42;
[b] H.L. Mobley, R.P. Hausinger, Microbiol. Rev. 53 (1989) 85–108;
[c] M.J. Maroney, S. Ciurli, Chem. Rev. 114 (2014) 4206–4228;
[d]L. Mazzei, F. Musiani, S. Ciurli, in *The Biological Chemistry of Nickel* (Eds.: D. Zamble, M. Rowińska-Żyrek, H. Kozłowski), Royal Society of Chemistry, **2017**, pp.

60–97. [e] L. Mazzei, F. Musiani, S. Ciurli, J. Biol. Inorg. Chem. 25 (2020) 829–845;
[f]L. Mazzei, S. Ciurli, in Encycl. Inorg. Bioinorg. Chem., John Wiley & Sons, Ltd, Chichester (UK), 2021, pp. 1–17.
[2] a J.C. Rutherford, PLoS Pathog. 10 (2014) e1004062;
b I. Konieczna, P. Zarnowiec, M. Kwinkowski, B. Kolesinska, J. Fraczyk, Z. Kaminski, W. Kaca, Curr. Protein Pept. Sci. 13 (2012) 789–806.
[3] a P. Bauerfeind, R. Garner, B.E. Dunn, H.L.T. Mobley, Gut 40 (1997) 25–30;
b B. Marshall, J.R. Warren, Lancet 323 (1984) 1311–1315.
[4] C. Zhou, F. Bhinderwala, M.K. Lehman, V.C. Thomas, S.S. Chaudhari, K.J. Yamada, K.W. Foster, R. Powers, T. Kielian, P.D. Fey, PLoS Pathog. 15 (2019) e1007538.
[5] W. Lin, V. Mathys, E.L.Y. Ang, V.H.Q. Koh, J.M.M. Gómez, M.L.T. Ang, S.Z. Z. Rahim, M.P. Tan, K. Pethe, S. Alonso, Infect. Immun. 80 (2012) 2771–2779.
[6] G.M. Cox, J. Mukherjee, G.T. Cole, A. Casadevall, J.R. Perfect, Infect. Immun. 68 (2000) 443–448.
[7] G. Young, D. Amid, V. Miller, J. Bacteriol. 178 (1996) 6487–6495.
[8] a S. Benini, W.R. Rypniewski, K.S. Wilson, S. Miletti, S. Ciurli, S. Mangani, Structure 7 (1999) 205–216;
b S. Benini, W.R. Rypniewski, K.S. Wilson, S. Ciurli, S. Mangani, Journal of biological inorganic chemistry : JBIC : a publication of the Society of Biological, Inorganic Chemistry 6 (2001) 778–790;
c S. Benini, W.R. Rypniewski, K.S. Wilson, S. Mangani, S. Ciurli, J Am Chem Soc 126 (2004) 3714–3715;
d S. Benini, M. Cianci, L. Mazzei, S. Ciurli, J. Biol. Inorg. Chem. 19 (2014) 1243–1261;
e L. Mazzei, M. Cianci, U. Contaldo, F. Musiani, S. Ciurli, Biochemistry 56 (2017) 5391–5404;
f L. Mazzei, M. Cianci, S. Benini, S. Ciurli, Chem. Eur. J. 25 (2019) 12145–12158;
g L. Mazzei, M. Cianci, S. Benini, S. Ciurli, Angew. Chem. Int. Ed. Engl. 58 (2019) 7415–7419;
h L. Mazzei, M. Cianci, U. Contaldo, S. Ciurli, J. Agric. Food Chem. 67 (2019) 2127–2138.
[9] L. Mazzei, A. Paul, M. Cianci, M. Devodier, D. Mandelli, P. Carloni, S. Ciurli, J. Inorg. Biochem. 250 (2024) 112398.
[10] [a] S. Benini, W.R. Rypniewski, K.S. Wilson, S. Ciurli, S. Mangani, J. Biol. Inorg. Chem. 3 (1998) 268–273;
[b] S. Ciurli, S. Benini, W.R. Rypniewski, K.S. Wilson, S. Miletti, S. Mangani, Coordination Chemistry Reviews 190–192 (1999) 331–355;
[c]S. Benini, W. R. Rypniewski, K. S. Wilson, S. Miletti, S. Ciurli, S. Mangani, *J. Biol. Inorg. Chem.* **2000**, *5*, 110–118. [d] L. Mazzei, M. Cianci, S. Benini, L. Bertini, F. Musiani, S. Ciurli, J. Inorg. Biochem. 154 (2016) 42–49.
[11] L. Mazzei, M. Cianci, F. Musiani, S. Ciurli, Dalton Trans. 45 (2016) 5455–5459.
[12] a L. Mazzei, M. Cianci, F. Musiani, G. Lente, M. Palombo, S. Ciurli, J Inorg Biochem 166 (2017) 182–189;
b L. Mazzei, U. Contaldo, F. Musiani, M. Cianci, G. Bagnolini, M. Roberti, S. Ciurli, Angew. Chem. Int. Ed. Engl. 60 (2021) 6029–6035.
[13] L. Mazzei, M. Cianci, S. Ciurli, Chemistry 28 (2022) e202201770.
[14] K. Macegoniuk, W. Tabor, L. Mazzei, M. Cianci, M. Giurg, K. Olech, M. Burda-Grabowska, R. Kaleta, A. Grabowiecka, A. Mucha, S. Ciurli, Ł. Berlicki, J. Med. Chem. 66 (2023) 2054–2063.
[15] a L. Mazzei, M. Cianci, A. Gonzalez Vara, S. Ciurli, Dalton Trans. 47 (2018) 8240–8247;
b L. Mazzei, D. Cirri, M. Cianci, L. Messori, S. Ciurli, J. Inorg. Biochem. 218 (2021) 111375.
[16] a L. Mazzei, M.N. Wenzel, M. Cianci, M. Palombo, A. Casini, S. Ciurli, A.C.S. Med, Chem. Lett. 10 (2019) 564–570;
b L. Mazzei, L. Massai, M. Cianci, L. Messori, S. Ciurli, Dalton Trans. 50 (2021) 14444–14452.
[17] a A. Balasubramanian, K. Ponnuraj, J. Mol. Biol. 400 (2010) 274–283;
b A. Balasubramanian, V. Durairajpandian, S. Elumalai, N. Mathivanan, A. K. Munirajan, K. Ponnuraj, Int. J. Biol. Macromol. 58 (2013) 301–309.
[18] a E. Jabri, M.B. Carr, R.P. Hausinger, P.A. Karplus, Science 268 (1995) 998–1004;
b E. Jabri, P.A. Karplus, Biochemistry 35 (1996) 10616–10626;
c M.A. Pearson, L.O. Michel, R.P. Hausinger, P.A. Karplus, Biochemistry 36 (1997) 8164–8172;
d M.A. Pearson, R.A. Schaller, L.O. Michel, P.A. Karplus, R.P. Hausinger, Biochemistry 37 (1998) 6214–6220;
e M.A. Pearson, I.S. Park, R.A. Schaller, L.O. Michel, P.A. Karplus, R.P. Hausinger, Biochemistry 39 (2000) 8575–8584;
f I.S. Park, L.O. Michel, M.A. Pearson, E. Jabri, P.A. Karplus, S. Wang, J. Dong, R. A. Scott, B.P. Koehler, M.K. Johnson, R.P. Hausinger, J. Biol. Chem. 271 (1996) 18632–18637;
g K. Yamaguchi, N.J. Cosper, C. Stalhandske, R.A. Scott, M.A. Pearson, P. A. Karplus, R.P. Hausinger, J. Biol. Inorg. Chem. 4 (1999) 468–477.
[19] P.A. Karplus, M.A. Pearson, R.P. Hausinger, Acc. Chem. Res. 30 (1997) 330–337.
[20] R.D. Righetto, L. Anton, R. Adaixo, R.P. Jakob, J. Zivanov, M.A. Mahi, P. Ringler, T. Schwede, T. Maier, H. Stahlberg, Nat. Commun. 11 (2020) 5101.
[21] E.S. Cunha, X. Chen, M. Sanz-Gaitero, D.J. Mills, H. Luecke, Nat. Commun. 12 (2021) 230.
[22] J.R. Feathers, K.A. Spoth, J.C. Fromme, J Struct Biol X 5 (2021) 100047.
[23] A.J. Jakobi, M. Wilmanns, C. Sachse, Elife (2017) 6.
[24] S. Benini, S. Ciurli, W.R. Rypniewski, K.S. Wilson, S. Mangani, Acta Crystallogr. D Biol. Crystallogr. 54 (1998) 409–412.
[25] A. Punjani, J.L. Rubinstein, D.J. Fleet, M.A. Brubaker, Nat. Methods 14 (2017) 290–296.
[26] A. Punjani, H. Zhang, D.J. Fleet, Nat. Methods 17 (2020) 1214–1221.
[27] E.C. Meng, T.D. Goddard, E.F. Pettersen, G.S. Couch, Z.J. Pearson, J.H. Morris, T. E. Ferrin, Protein Sci. 32 (2023) e4792.
[28] P.V. Afonine, B.K. Poon, R.J. Read, O.V. Sobolev, T.C. Terwilliger, A. Urzhumtsev, P.D. Adams, Acta Crystallogr D Struct Biol 74 (2018) 531–544.
[29] T.C. Terwilliger, O.V. Sobolev, P.V. Afonine, P.D. Adams, Acta Crystallogr D Struct Biol 74 (2018) 545–559.
[30] a P. Emsley, K. Cowtan, Acta Crystallogr D Biol Crystallogr 60 (2004) 2126–2132;
b P. Emsley, B. Lohkamp, W.G. Scott, K. Cowtan, Acta Crystallogr. D Biol. Crystallogr. 66 (2010) 486–501.
[31] C. Wood, T. Burnley, A. Patwardhan, S. Scheres, M. Topf, A. Roseman, M. Winn, Acta Crystallogr. Sect. D 71 (2015) 123–126.
[32] V.B. Chen, W.B. Arendall 3rd, J.J. Headd, D.A. Keedy, R.M. Immormino, G. J. Kapral, L.W. Murray, J.S. Richardson, D.C. Richardson, Acta Crystallogr. D Biol. Crystallogr. 66 (2010) 12–21.